UC Berkeley

Title

Octahedral Distortion and Excitonic Behavior of $Cs_3Bi_2Br_9$ Halide Perovskite at Low Temperature

Authors

Jin, Jianbo
Quan, Li Na
Gao, Mengyu
et al.

Peer reviewed

Octahedral Distortion and Excitonic Behavior of $Cs_3Bi_2Br_9$ Halide Perovskite at Low Temperature

Jianbo Jin[1,#], Li Na Quan[2,5,#], Mengyu Gao[3], Chubai Chen[1], Peijun Guo[6], and Peidong Yang[*,1,2,3,4]

1 Department of Chemistry, University of California, Berkeley, California 94720, United States

2 Materials Sciences Division, Lawrence Berkeley National Laboratory, Berkeley, California 94720, United States

3 Department of Materials Science and Engineering, University of California, Berkeley, California 94720, United States

4 Kavli Energy NanoScience Institute, Berkeley, California 94720, United States

5 Department of Chemistry, Virginia Tech, Virginia 24061, United States

6 Department of Chemical and Environmental Engineering, Yale University, New Haven, 06520, United States

[#] J.J. and L.N.Q. contributed equally

[*] Corresponding author. Email: p_yang@berkeley.edu (P.Y.)

Keywords: Low dimensional perovskites, exciton, octahedron distortion

ABSTRACT

The metal halide ionic octahedron, represented as $[MX_6]^{n-}$ (M = metal cation, X = halide anion), serves as the basic structural unit in metal halide perovskites and plays a crucial role in determining their optoelectronic and chemical properties. Thus, it is possible to correlate the responses of metal halide perovskites to various environmental stimuli with the dynamic behaviors of the individual octahedra that make up these materials. In this study, with the temperature dependent single crystal-XRD measurements on $Cs_3Bi_2Br_9$ 2D halide perovskites, we can identify two classes of distortions through the lowering of temperature: *Intra-octahedral distortion* – the off-centering of Bi atoms within the $[BiBr_6]^{3-}$ octahedron due to the Bi $6s^2$ lone pair electrons, and *Inter-octahedral distortion* – the collective misalignments among the $[BiBr_6]^{3-}$ octahedra building blocks. Free exciton (FE) and self-trapped exciton (STE) models are used to study the relationship between the distortion of octahedra in $Cs_3Bi_2Br_9$ and the corresponding changes in its optoelectronic properties, which transform from dominating blue emission above 100 K to red emission at 4 K. This work provides new insights into the excitonic behavior of perovskite building blocks and suggests the possibility that we can design and rationalize the optical properties by regulating the environmental stimuli with the knowledge of the behaviors of the individual building blocks.

INTRODUCTION

Metal halide perovskites is a new family of semiconductor materials that have been extensively studied in the past decade due to their superior optoelectronic properties[1–3] and rich structures.[4,5] The prototype metal halide perovskites are in the formula of AMX_3 (where A = MA^+, Cs^+, Rb^+, etc., M = Pb^{2+}, Sn^{2+}, Ge^{2+}, etc., and X = Cl^-, Br^-, and I^-), which is built up by the corner-sharing $[MX_6]^{n-}$ metal halide ionic octahedron. Such ionic octahedra are the basic structural and functional units of metal halide perovskites.[6] The assembly, connection, and interaction of octahedra in metal halide perovskites are critical to create novel optical, electronic and chemical properties.[7] Thus, fundamental understanding of the behavior of $[MX_6]^{n-}$ octahedron is essential for establishing a basis for the rational synthesis and potential applications of metal halide perovskites.

The optoelectronic properties of metal halide perovskites can be regulated by various environmental stimuli, such as temperature,[8–11] electrical field,[12–14] and pressure.[15–18] These properties are believed to be related to the behavior of individual octahedra within the material, as the soft lattice nature of metal halide perovskites allows for changes in the packing, connectivity, and configuration of $[MX_6]^{n-}$ octahedra in response to the external stimuli.[19] One example of this is the distortion of $[MX_6]^{n-}$ octahedra that occurs with temperature changes, as seen in the tilting and misalignments of $[PbBr_6]^{4-}$ octahedra in 3D and 2D lead halide perovskites.[20–23] Specifically, the corner-sharing $[PbBr_6]^{4-}$ octahedra become increasingly tilted when $CsPbBr_3$ goes from the cubic phase (Pm-3m, T > 130℃), to the tetragonal phase (P4/mbm, 88℃ < T < 130℃), and then the orthorhombic phase (Pnma, T < 88℃).[20] The tilting of $[PbBr_6]^{4-}$ octahedra can influence the orbital overlaps and change the electronic structures.[24,25] In

3

addition to the tilting among a collection of octahedra, distortions also happen within an individual octahedron, such as off-centering of the center metal sites, and Jahn-Teller distortions. With the existence of ns^2 lone pair electrons, metal cations like Ge^{2+},[26] Sn^{2+},[27] Sb^{3+},[28,29] Bi^{3+},[30,31] Te^{4+},[32–34] etc. would show off-centering for the metal cations under certain conditions. The carrier dynamics and photoluminescence of metal halide perovskites with those M^{n+} cations are heavily dependent on the off-centering and dynamics of the ns^2 lone pair electrons.[27,31–33] For example, the off-centering of the Ge^{2+} in $[GeBr_6]^{4-}$ octahedron contributes to the ferroelectricity of the $CsGeBr_3$.[26] And the emission and the molecule-like absorbance features of Cs_2TeCl_6 can be understood with the dynamic Jahn-Teller distortions of $[TeCl_6]^{2-}$ ionic octahedron.[35] Thus, it is possible to correlate the responses of metal halide perovskites to various environmental stimuli with the dynamic behavior of the individual octahedra building blocks. To better illustrate the nature of different kinds of metal halide octahedron distortions, we can classify them into two families of distortions: *Intra-octahedral distortion* – where the distortion happens within an octahedron, and *Inter-octahedral distortion* – where the distortion happens among a collection of octahedra.

Vacancy-ordered halide perovskites, including $Cs_2M(IV)X_6$ and $Cs_3M(III)_2Br_9$, are formed with vacancies on the Pb^{2+} sites based on the prototype $CsPb(II)X_3$ halide perovskites.[36] Due to low electronic dimensionality and strong exciton-phonon coupling, these low-dimensional halide perovskites can exhibits broad outstanding broad emission properties, which are originated from radiatively decay of the self-trapped excitons (STEs). [33,37–39] Studies have shown that among these vacancy-ordered halide perovskites, $Cs_3Bi_2Br_9$ (CBB) displays two distinct emissions that can be attributed to the emissions of STEs and free excitons (FEs), respectively.[37,40] As a result, the CBB would be a great platform to study how the excitonic

4

behaviors of halide perovskites can be understood from the distortions of the $[BiBr_6]^{2-}$ octahedra. While scientists have studied the mechanisms for the two emissions from bulk CBB, there are significant research gaps in its structural transformations and changes in excitonic behaviors at low temperature. Understanding the excitonic behaviors of metal halide perovskites is crucial to study the nature of their optical responses as well as their applications.[41]

In this study, CBB is selected as a case study to investigate the relationship between structural distortions and optoelectronic properties of 2D halide perovskites. Through *in situ* single crystal X-ray diffraction (SCXRD), two kinds of distortions of the $[BiBr_6]^{3-}$ octahedron within the CBB lattices are identified upon lowering of temperature: *Intra-octahedral distortion*, which involves the off-centering of Bi atoms within $[BiBr_6]^{3-}$ octahedron, and *Inter-octahedral distortion*, which refers to the collective misalignments among the $[BiBr_6]^{3-}$ octahedra. Temperature-dependent optical measurements reveal that the excitonic luminescence of CBB changes from a dominant blue emission (462 nm) at temperatures above 100 K to a broad and red emission (550-750 nm) at 4 K. The FE and STE models are applied to study the correlation between the distortion of $[BiBr_6]^{3-}$ octahedron and the changes in optoelectronic properties of CBB. Through this investigation, we are able to establish a structure-property relationship by gaining a comprehensive understanding of the dynamic behaviors of $[BiBr_6]^{3-}$ octahedra in CBB.

EXPERIMENTAL METHODS

Materials. CsBr (99.999%, Sigma Aldrich), $BiBr_3$ (99.998%, Sigma Aldrich), and HBr (Sigma Aldrich, reagent grade, 48%) were used as received without further purification or modification.

Synthesis of Cs₃Bi₂Br₉ single crystals. $Cs_3Bi_2Br_9$ single crystals were synthesized using the HBr solution methods. Typically, 0.05mmol $BiBr_3$ and 0.75mmol CsBr were dissolved in 1.0mL HBr to yield a light-yellow clean solution. The solution was heated at 80℃ and then kept at room temperature. Thick octahedral-shaped crystals in size of about 200 μm were crystalized out by keeping this solution overnight. However, we found the thick crystals will result in poor R_{int} values for the SCXRD. Instead, we used HBr evaporation methods for thinner crystals for SCXRD. 100μL solution was dropped onto a glass slide and got fully dried by hot plates. The thin crystals are shown in **Figure S1**. Thick single crystals were exfoliated with 3M scotch tape to very thin layers for PL measurements.

Powder X-ray Diffraction. Powder X-ray diffraction (PXRD) data is collected using a Bruker D8 laboratory diffractometer with a Cu Kα radiation source in ambient conditions. Data is collected from 2θ = 7° to 60°. The single crystals are ground into powders and transferred onto the glass for measurements.

Single-Crystal X-ray Diffraction (SCXRD). The SCXRD data was collected at the Small Molecule X-ray Crystallography Facility (CheXray) at the College of Chemistry, UC Berkeley. SCXRD was measured with a Rigaku XtaLAB P200 instrument equipped with a MicroMax-007 HF microfocus rotating anode and a Pilatus 200 K hybrid pixel array detector using monochromated Cu Kα radiation (λ = 1.54184Å). All crystal datasets were collected at the same piece of crystal (**Figure S2**). CrysAlisPro[42] was used for data collection and data processing, including a multi-scan absorption correction applied using the SCALE3 ABSPACK scaling algorithm. Unwarp images were also generated with the CrysAlisPro. Using Olex2[43], the

6

structures were solved with the SHELXT[44] structure solution program using Intrinsic Phasing and refined with the SHELXL[45] refinement package using Least Squares minimization.

Optical Microscope Imaging. An unpolarized, white-light optical microscope was used to visualize single crystals under either a 20× or a 50× microscope objective. $Cs_3Bi_2Br_9$ crystals were observed under dark-field imaging. The single crystals were dispersed onto the glass for measurement.

Scanning Electron Microscopy and Energy-Dispersive X-ray Spectroscopy. A field-emission SEM (FEI Quanta 3D FEG SEM/FIB) was used to visualize single crystal morphologies and to determine atomic ratios in the single crystals via the EDX detector.

Temperature-dependent Raman Spectroscopy. The Raman spectra of the samples were measured at Sector 13 (GeoSoilEnviroCARS, University of Chicago, IL) of the Advanced Photon Source (APS), Argonne National Laboratory (ANL), using a custom-built con confocal Raman microscope system with 660 nm laser excitation.[46] Solid-state volume Bragg filters equipped on the system permit the measurement of Raman peaks down to about 5 cm^{-1}. The single crystals were dispersed onto glass microscope slides for measurement. The laser was focused onto a crystal facet at a constant power density (<2 mW) set by neutral density filters. The Raman signal from the sample was collected using a Mitutoyo microscope objective in a back-scattering geometry (20 ×, NA 0.42). The high-resolution Raman spectra were measured with a CCD detector and a Princeton Instruments Acton Series 2500 (focal length = 500 mm) equipped with a diffraction grating of 1200 gr/mm.

PL Spectroscopy. All photoluminescence-related measurements, including standard PL and PL microscope imaging, were collected with a home-built PL microscope system. The single

7

crystals were exfoliated onto the SiO_2 substrate and conducted PL measurements. A continuous-wave solid-state 375 nm laser (Coherent OBIS 375LX) was focused obliquely onto the sample with a constant power density in visible wavelength measurements, which was set by neutral density filters. The PL signal from the sample was collected using a microscope objective (50×) coupled to a long-pass filter (390 nm) to remove the laser line from the signal. PL spectra were collected under a 1 s exposure time with a Si CCD detector cooled to -120℃ via liquid nitrogen and equipped with a diffraction grating of 150 gr/mm. The PL imaging was taken under bright-field conditions. Low-temperature PL measurement was measured in the same PL microscope system coupled with a microscope cryostat (Janis Research, ST-500). Samples were held inside the cryostat under vacuum ($5×10^6$ torr) and cooled to 4 K with liquid He. The incident excitation laser beam was focused onto the sample through a transparent quartz window. The spectra were taken by the grating-based spectrograph.

Density Function Theory (DFT) Calculations. The electronic band structures of $Cs_3Bi_2Br_9$ at 200 K, 90 K, and 19 K were calculated by DFT calculations with the CASTEP[47] code implemented in the Materials Studio 2020. The norm conserving pseudopotential[48] was applied for electron interactions in metal halides. All three structures models were imported from CIF files, and the geometry optimization has been applied with PBE+GGA[49]. A fine frame was chosen for energy cutoffs and calculation quality. Electronic band structures and partial density of states (pDOS) were calculated with PBE+GGA without spin-orbital coupling (SOC). Electronic band structures were further calculated with PBE+GGA with the SOC effects.

Molecular Orbitals Calculations. The molecular orbitals of $[BiBr_6]^{3-}$ octahedron in O_h and C_{3v} point groups were calculated with the Gaussian engine implemented in WebMO.[50] The

octahedral models were imported in XYZ format, with structural parameters listed in **Tables S7** and **S8**. The calculations were carried out with B3LYP[51] theory and SDD basis set. The charge was set to -3 and the spin multiplicity was set to the singlet.

RESULTS AND DISCUSSION

$Cs_3Bi_2Br_9$ (CBB) is a layered metal halide perovskite that two-thirds of the M^{2+} sites are occupied by Bi^{3+} cations, with layers of vacancies on metal sites formed along the <110> directions (**Figure 1a**). Thin CBB crystals are synthesized by the typical HBr evaporation crystallization process for later characterizations. The phase and the composition of the formed crystals are confirmed through the PXRD, SEM images and the EDS spectra, as shown in **Figures S1 and S2**. While phase transitions at different temperatures have been extensively studied in $CsPbX_3$, the low-temperature structure studies on CBB are still lacking. To quantitatively investigate the configurations of $[BiBr_6]^{3-}$ metal halide octahedra upon cooling, SCXRD is applied on a thin plate-shaped CBB crystal ($0.024 \times 0.069 \times 0.074$ mm), using the liquid nitrogen (LN_2) stream for cooling. All crystallographic tables are summarized in **Tables S1 and S2**. The SCXRD results reveal that an off-centering distortion occurs within $[BiBr_6]^{3-}$ octahedron as the temperature is lowered from 293K to 100 K, while maintaining a P-3m1 trigonal lattice. The rising of the off-centering distortion is due to the presence of Bi $6s^2$ lone pair electrons. This distortion occurs within the individual octahedron and repeats periodically within the entire lattice space, without resulting a supercell formation since the octahedra are still perfectly lined up along the *c* axis of the unit cell. Therefore, we designate this off-centering as an *intra-octahedral distortion*.

Figure 1b shows the intra-octahedral distortion happens along the *c* axis of the hexagonal unit cell. To investigate this distortion upon cooling, an off-centered octahedron model, as depicted in **Figure 1c,** is applied. The Bi $6s^2$ lone pair electrons polarized along the 3-fold axis of an O_h $[BiBr_6]^{3-}$ octahedron, which is the same as the Ge $4s^2$ long pair electrons in $[GeBr_6]^{4-}$

10

octahedra within $CsGeBr_3$.[26] As a result, the $[BiBr_6]^{3-}$ octahedra within lattice exhibit in C_{3v} symmetry rather than O_h point group symmetry, and the six Br atoms are no longer symmetrically identical. Two different types of Br atoms, labeled as Br1 and Br2, as distinguished, where Br1 represents the external Br atom and Br2 represents the shared Br atom which bridges two corner-sharing $[BiBr_6]^{3-}$ units. **Figures 1d and 1e** summarize the quantitative structural analysis from room temperature to 100 K. Along the cooling, the lattice parameters are found to decrease linearly from 7.9605 Å to 7.8841 Å for *a*, and from 9.8458 Å to 9.7793 Å for *c*, indicating that no phase transition takes place in this temperature region. **Figures 1f and 1g** depict the variations in the Bi-Br1 and Bi-Br2 bond lengths. Interestingly, it is noteworthy that the Bi-Br1 bond length remains relatively constant, while the Bi-Br2 bond length demonstrates a linear decrease. This observation implies that the lone pair electron end is more flexible when the lattice is shrunken. To quantify the Bi^{3+} off-centering, the octahedron scales (*L*) is calculated as the average of atomic distances of Br1a-Br2a, Br1b-Br2b, and Br1c-Br2c. The off-centering vectors (d_{oc}) represents the displacement from the real Bi atom Cartesian coordinates to the theoretical octahedron center, which is exactly the middle point of Br1a-Br2a, Br1b-Br2b, and Br1c-Br2c. The *intra-octahedral distortion* can be quantified by utilizing the ratio of off-centering vectors to the octahedron scales ($d_{oc}\% = d_{oc} / L$). As the lattice is compressed upon cooling, the $d_{oc}\%$ increases from 0.2167 Å to 0.2258 Å, with *L* decreasing from 5.6740 Å to 5.5693 Å. This results in a linear increase of the *intra-octahedral distortion* ($d_{oc}\%$) from 3.819% to 3.990% (**Figure 1h**). All details of the calculation are covered in **Table S5**.

The *inter-octahedral distortion* is also observed in the *in situ* temperature-dependent SCXRD experiments. While phase transitions at different temperatures have been extensively

studied in CsPbX$_3$, the low-temperature structure studies on CBB are still lacking. Nuclear quadrupole resonance (NQR) spectra indicated that CBB undergoes a phase transition at approximately 90 K.[11] Furthermore, an additional x-ray scattering peak can be observed between the (1,0,8) and (1,0,9) Bragg peaks of the prototype trigonal unit cell of CBB at 80 K.[11] To experimentally confirm the existence of the phase transition, SCXRD measurement at 90 K is conducted to the same CBB crystal. Intriguingly, the raw data reveals the presences of a doubled trigonal unit cell. Unwarp images built on (100) and (001) layers on raw diffraction frames of experiments at 100 K and 90 K are displayed in **Figures 2a** and **2b**. These figures demonstrate the presences of additional diffractions (highlighted in the white boxes) that correspond to the *c*-doubled super unit cell. The zoomed images clearly show the (1,0,2.5) and (1,0,8.5) diffractions, which correspond to the (1,0,5) and (1,0,17) facets in the doubled unit cell. These extra diffractions are also present in the unwarp images built on (010) and (001) layers (**Figures S4a** and **S4b**). However, no extra diffractions have been shown in the unwarp images built on (100) and (001) layers, indicating that there is no unit cell doubling along the *a*- and *b*-axes (**Figures S4c** and **S4d**). As a result, a *c*-doubled P-3m1 trigonal unit-cell with dimensions of *a* = 7.8804 Å and *c* = 19.5572 Å has been determined from the dataset (labeled **90 K-doubled** in **Table S3**). The adjacent two layers of [BiBr$_6$]$^{3-}$ octahedra within **90 K-doubled** CBB unit cell are no longer identical, which is shown in blue and red in **Figure 2c**. The degrees of off-centering for the two octahedra (d_{oc}%) are calculated as 3.874% and 4.125%, respectively (details in **Table S6**).

It is worth noting that the temperature of 90 K is close the capability of the LN$_2$ stream cooling system to keep the temperature safe and stable in SCXRD measurements. Additionally, all additional peaks observed at 90 K remain relatively weak. Therefore, the crystal structure can

still be solved, or in another word, averaged in the prototype P-3m1 trigonal unit cell with dimensions of a = 7.8800 Å and c = 9.7789 Å (as labeled **90 K-prototype** in **Table S3**), referring to a smaller R_1 and wR_2 residue parameters. The $d_{oc}\%$ is calculated as 3.997% in this averaged unit cell. However, with the clear differences observed in the 90 K unwarp images, we have experimentally proved that a phase transition occurs from 100 K to 90 K, and the two layers of $[BiBr_6]^{3-}$ octahedra in the c-doubled unit cell are no longer crystallographically identical. Furthermore, **Figure 3** shows the octahedra are still perfectly aligned along the c-direction at 90 K (**Figure 3**). This phase transition is caused by the differences in the level of *intra-octahedral distortion* between the two connected $[BiBr_6]^{3-}$ octahedra. It is assumed that the lowering of symmetry and changes in *intra-octahedral distortion* occur prior to any changes the *inter-octahedral distortion* as the temperature decreases. Low-T Raman spectroscopy also shows the lattice at 78K retrains the stretching vibrational modes of $Bi_2Br_9^{3-}$ as same as the room temperature structures (**Figure S5**).

The *inter-octahedral distortion* is also observed in the *in situ* temperature-dependent SCXRD experiments at temperatures below 90 K. A monoclinic unit cell of CBB (ICSD: 96723)[11] with dimensions of a = 13.6750 Å, b = 7.8593 Å, and c = 19.5572 Å has been reported at 19 K. **Table S4** summarizes the crystallographic details of the monoclinic unit cell, which is 4 times larger in volume compared to the prototype P-3m1 unit cell at room temperature. **Figure 3** illustrates the side views and top views of the three CBB unit cell models. It is evident that the $[BiBr_6]^{3-}$ are no longer perfectly aligned at 19 K, indicating that *inter-octahedral distortion* occurs upon cooling from 90 K to 19 K. The transformation from the P-3m1 unit cell to c-doubled P-3m1 unit cell, and to the quadruple monoclinic C2/c unit cell demonstrates an

13

increasing degree of octahedral distortions within and among octahedra with decreasing temperature. In summary, the well aligned $[BiBr_6]^{3-}$ become increasingly distorted when the temperature is lower than 90 K, and the symmetry of the lattice decreases from the trigonal into a monoclinic symmetry.

The electronic band structures and optoelectronic properties of halide perovskites are closely related to the dynamic behaviors of $[MX_6]^{n-}$ octahedra that make up the materials. As demonstrated by Shi *et al.*, CBB exhibits two distinct emission peaks: a blue emission referring to the near band edge emissions of FEs, and a broad near-infrared (NIR) emission that is attributed to the radiative decay of STEs.[37] This broad emission is proved to be not associated with the defect-assisted processes as the same life time is observed on CBB powders and high-quality single crystals from the time-resolved photoluminescence (TRPL) measurements.[37] Low-temperature optical measurements are conducted on exfoliated thin CBB crystals. Both FE and STE emissions are observed in the temperature-dependent PL measurements (**Figure 4a**). At room temperature, a weak emission at about 470 nm is observed, which is very close to the direct bandgap transition from CBB, as determined to be 2.64 eV from the Tauc plot (**Figures S6b** and **S6c**). This band edge FE also contributes to an exitonic absorption peak in the absorption spectrum (**Figure S6a**). Upon cooling of CBB from room temperature to 100 K, the blue emission centered at 463 nm becomes stronger. At the temperature of 60 K, a shoulder FE emission centered at 450 nm emerges, and it becomes more significant at 40 K and lower temperature. (**Figure 4b**). On the other hand, at the temperature around 200 K, the broad NIR STE emission centered around 720 nm emerges, characterized with a significant stokes shift and a broad full width at half maximum (FWHM). The center of the STE emission shifts slightly to

14

737 nm at 100 K, and the intensity of the STE emission becomes much stronger. At 60 K, the STE emission remains similar, but the center shifts further to 770 nm. At the temperature of 40 K, another broad red emission peak centered at 643 nm appears, which becomes the dominant emission peak at 10 K and 4 K. In addition, the intensity of STE emission vs FE emission increases as the temperature deceases. As a result, the emission of CBB changes from dominating blue emission above 100 K (**Figure 4c**) to red emission at 4 K (**Figure 4d**).

To gain insights into the splitting and changes observed in the emission spectra, density function theory (DFT) calculations are performed on three CBB models (200 K, 90 K, and 19 K) with different levels of *intra-octahedral* and *inter-octahedral distortions*. Electronic band structures and partial density of states (pDOS) are calculated using the GGA-PBE functional without spin-orbital coupling (SOC) effects (**Figure S7**). The valence band edge of CBB is contributed by Bi 6s and Br 4p electrons, while the conduction band edge composed by Bi 6p and Br 4p electrons. This is in great agreement with the highest occupied molecular orbitals (HOMO) and lowest unoccupied molecular orbitals (LUMO) of the $[BiBr_6]^{3-}$ octahedron, respectively (**Table S4** and **S5**, **Figure S7**). SOC effects are included in the band structure calculations to reveal the band dispersions of the system composed of heavy atoms. The band structures of the prototype P-3m1 structures (200 K) and the *c*-doubled P-3m1 unit cell at 90 K are shown in **Figure 5a** and **5b**. Since the *c*-doubled cell preserves the trigonal symmetry, the band structure of 90 K exhibits a similar structure, but with twice the number of energy bands after folding along the k-space. A small energy gap appears at the Γ point, due to the SOC effect. **Figure 5c** illustrates that the degenerated energy bands are split into two conduction band fronts at 19 K. This results in the emergence of the new FE emission at 450 nm. The STE emission

peaks exhibits in a continuous trend from room temperature to 60 K, despite the occurrence of a phase transition at 90 K. This suggests that the *c*-doubled trigonal structure after phase transition does not significantly alter the nature of the STE states, as STE is dependent on the electron-phonon coupling and the phonon dispersion remains similar when the structure is still in a trigonal symmetry. However, due to the phase transition, when the temperature in between 100K to 60K, the emission shifts from 737 nm to 770 nm is greater than the shifts observed above 100 K. The emergence of a new broad red emission at 40 K should correspond to the well-aligned $[BiBr_6]^{3-}$ bilayers in the trigonal phase Model 2, due to a phase transition into the misaligned $[BiBr_6]^{3-}$ bilayers in the unit cell of Model 3 (**Figure 3**). This suggests a phase transition from the *c*-doubled trigonal unit cell to monoclinic unit cell occurs at the temperature around 60 K and 40 K, with an increased degree of the *inter-octahedral distortion*.

The intensities of both FE and STE emissions are increased when the temperature cools from room temperature to 100 K, while the CBB lattices remains in the prototype P-3m1 phase. This enhancement can be attributed to the reduction in exciton dissociation caused by the decrease in temperature, leading to an increase in intensity for both FE and STE emissions. Additionally, the STE emission is found to be more prominent compared to the FE emission at 100 K. The *intra-octahedral distortion* within the $[BiBr_6]^{3-}$ octahedron leads to a strong exciton-phonon coupling in CBB.[30] This results in the STE of CBB being more susceptible to non-radiative recombination at room temperature.[37] Therefore, as the temperature is lowered, the non-radiative thermal quenching of STE is suppressed, and as a result, STE emissions increases more significantly. At temperatures below 60 K, the STE emission remains stronger compared to the FE emission, which can be attributed to the presence of *intra-octahedral distortion*. Smith *et al.*

report that the intensities of FE and STE emissions are closely correlated with octahedron distortion.[22] They report that a stronger STE:FE intensity ratio is achieved with a greater degree of tilting of $[PbBr_6]^{4-}$ octahedra long the z axes in 2D A_2PbBr_4 crystals, either triggered by organic cations or the lowering of temperature.[22] Similarly, the *inter-octahedral distortion* in the monoclinic lattice can provide more intrinsic lattice vibration and distortion for the FE to be trapped to the new STE states. **Figures 5d-f** illustrate the schematics for the FE and STE emissions for CBB at 200 K, 90 K and 19 K**.** In conclusion, the blue FE emission is stronger than the NIR STE emission on CBB at 200 K, as most of the STEs undergo a non-radiative recombination process. As the temperature decreases to 90 K, the STE emission significantly increases as the non-radiative recombination gets suppressed. Finally, at 4 K, the two conduction band edges contribute to two distinct FE emissions, while the new red STE emission dominates due to a higher level of octahedron distortions.

CONCLUSION

In this work, we are categorizing the distortions of metal halide octahedron in perovskites into two modes: *intra-octahedral distortion* and *inter-octahedral distortion*. We quantitatively analyze the structure of $Cs_3Bi_2Br_9$ (CBB) layered perovskites using *in situ* SCXRD from room temperature to 100 K and found the CBB keeps in the P-3m1 trigonal unit cell with the increase in the *intra-octahedral distortion* – Bi^{3+} off-centering within $[BiBr_6]^{3-}$ octahedron. The phase transition from original P-3m1 phase to the *c*-doubled trigonal phase is experimentally proved at 90 K. The temperature-dependent optical measurements reveal the changes in both free exciton (FE) and self-trapped exciton (STE) emissions, which results in the CBB blue emissive above 100 K and red emissive at 4 K. We use the understanding of the performances of $[BiBr_6]^{3-}$ octahedra to address and understand the complex excitonic behaviors of CBB. This work highlights the dynamic nature of the metal halide octahedra and it presents a new approach for studying the behaviors of halide perovskites under various environmental stimuli from the knowledge of the individual metal halide octahedra.

ASSOCIATED CONTENT

Supporting Information

The Supporting Information is available free of charge on the ACS Publications website at DOI:

Crystallographic tables of $Cs_3Bi_2Br_9$ structures at different temperature, details of molecular orbital calculation. Figures showing SEM and EDS results, Powder XRD, and Raman spectra, including Figures S1-S8, Tables S1-S8. (PDF)

Accession Code:

The crystallographic information file (CIF) has also been deposited in the Inorganic Crystal Structure Database under reference numbers CSD 2195436 – 2195442. These data can be obtained free of charge via https://www.ccdc.cam.ac.uk/structures/, or by emailing data_request@ccdc.cam.ac.uk.

Notes

The authors declare no competing financial interest.

AUTHOR INFORMATION

Corresponding Author

*Email: p_yang@berkeley.edu

ORCID

Jianbo Jin: 0000-0002-9054-7960

Li Na Quan: 0000-0001-9301-3764

Mengyu Gao: 0000-0003-1385-7364

Chubai Chen: 0000-0003-2513-2707

Peijun Guo: 0000-0001-5732-7061

Peidong Yang: 0000-0003-4799-1684

Author Contributions

The manuscript was written with contributions of all authors. All authors have given approval to the final version of the manuscript.

ACKNOWLEDGMENT

REFERENCES:

(1)   Manser, J. S.; Christians, J. A.; Kamat, P. v. Intriguing Optoelectronic Properties of Metal Halide Perovskites. *Chem. Rev.* **2016**, *116*, 12956–13008. https://doi.org/10.1021/acs.chemrev.6b00136.

(2)   Kovalenko, M. v; Protesescu, L.; Bodnarchuk, M. I. Properties and Potential Optoelectronic Applications of Lead Halide Perovskite Nanocrystals. *Science* **2017**, *358*, 745. https://doi.org/10.1126/science.aam7093.

(3)   Dey, A.; Ye, J.; De, A.; Debroye, E.; Ha, S. K.; Bladt, E.; Kshirsagar, A. S.; Wang, Z.; Yin, J.; Wang, Y. *et al.* State of the Art and Prospects for Halide Perovskite Nanocrystals. *ACS Nano*, **2021**, *15*, 10775–10981. https://doi.org/10.1021/acsnano.0c08903.

(4)   Steele, J. A.; Lai, M.; Zhang, Y.; Lin, Z.; Hofkens, J.; Roeffaers, M. B. J.; Yang, P. Phase Transitions and Anion Exchange in All-Inorganic Halide Perovskites. *Acc. Mater. Res.* **2020**, *1*, 3–15. https://doi.org/10.1021/accountsmr.0c00009.

(5)   Huang, J.; Lai, M.; Lin, J.; Yang, P. Rich Chemistry in Inorganic Halide Perovskite Nanostructures. *Adv. Mater.* **2018**, *30*, 1802856. https://doi.org/10.1002/adma.201802856.

(6)   Jin, J.; Folgueras, M. C.; Gao, M.; Yu, S.; Louisia, S.; Zhang, Y.; Quan, L. N.; Chen, C.; Zhang, R.; Seeler, F. *et al.* A New Perspective and Design Principle for Halide Perovskites: Ionic Octahedron Network (ION). *Nano Lett.* **2021**, *21*, 5415–5421. https://doi.org/10.1021/acs.nanolett.1c01897.

(7)   Zhu, C.; Jin, J.; Gao, M.; Oddo, A. M.; Folgueras, M. C.; Zhang, Y.; Lin, C.-K.; Yang, P. Supramolecular Assembly of Halide Perovskite Building Blocks. *J. Am. Chem. Soc.* **2022**, *144*, 12450–12458. https://doi.org/10.1021/jacs.2c04357.

(8)   Lin, J.; Lai, M.; Dou, L.; Kley, C. S.; Chen, H.; Peng, F.; Sun, J.; Lu, D.; Hawks, S. A.; Xie, C. *et al.* Thermochromic Halide Perovskite Solar Cells. *Nat. Mater.* **2018**, *17*, 261–267. https://doi.org/10.1038/s41563-017-0006-0.

(9)   Chen, H.; Lin, J.; Kang, J.; Kong, Q.; Lu, D.; Kang, J.; Lai, M.; Quan, L. N.; Lin, Z.; Jin, J. *et al.* Structural and Spectral Dynamics of Single-Crystalline Ruddlesden-Popper Phase Halide Perovskite Blue Light-Emitting Diodes. *Sci. Adv.* **2020**, *6*, eaay4045. https://doi.org/10.1126/sciadv.aay4045.

(10)   Bischak, C. G.; Lai, M.; Fan, Z.; Lu, D.; David, P.; Dong, D.; Chen, H.; Etman, A. S.; Lei, T.; Sun, J *et al.* Liquid-like Interfaces Mediate Structural Phase Transitions in Lead Halide Perovskites. *Matter* **2020**, *3*, 534–545. https://doi.org/10.1016/j.matt.2020.07.015.

(11)   Aleksandrova, I. P.; Burriel, R.; Bartolome, J.; Bagautdinov, B. Sh.; Blasco, J.; Sukhovsky, A. A.; Torres, J. M.; Vasiljev, A. D.; Solovjev, L. A. Low-Temperature Phase Transitions in the Trigonal Modification of $Cs_3Bi_2Br_9$ and $Cs_3Sb_2I_9$. *Phase Transitions* **2002**, *75*, 607–620. https://doi.org/10.1080/01411590290029863.

(12)   Chen, B.; Li, T.; Dong, Q.; Mosconi, E.; Song, J.; Chen, Z.; Deng, Y.; Liu, Y.; Ducharme, S.; Gruverman, A. *et al.* Large Electrostrictive Response in Lead Halide Perovskites. *Nat. Mater.* **2018**, *17*, 1020–1026. https://doi.org/10.1038/s41563-018-0170-x.

(13)   Leppert, L.; Reyes-Lillo, S. E.; Neaton, J. B. Electric Field- and Strain-Induced Rashba Effect in Hybrid Halide Perovskites. *J. Phys. Chem. Lett.* **2016**, *7*, 3683–3689. https://doi.org/10.1021/acs.jpclett.6b01794.

(14)   Gao, Y.; Li, X.; Liu, W.; Xing, X.; Long, H.; Wang, K.; Wang, B.; Lu, P. Highly Tunable Enhancement and Switching of Nonlinear Emission from All-Inorganic Lead Halide Perovskites

via Electric Field. *Nano Lett.* **2021**, *21*, 10230–10237. https://doi.org/10.1021/acs.nanolett.1c03142.

(15)   Liu, X. J.; Moritomo, Y.; Nakamura, A.; Kojima, N. Pressure-Induced Phase Transition in Mixed-Valence Gold Complexes $Cs_2Au_2X_6$ (X=Cl and Br). *J. Chem. Phys.* **1999**, *110*, 9174–9178. https://doi.org/10.1063/1.478839.

(16)   Lin, J.; Chen, H.; Gao, Y.; Cai, Y.; Jin, J.; Etman, A. S.; Kang, J.; Lei, T.; Lin, Z.; Folgueras, M. C. *et al.* Pressure-Induced Semiconductor-to-Metal Phase Transition of a Charge-Ordered Indium Halide Perovskite. *Proc. Natl. Acad. Sci. U. S. A.* **2019**, *116*, 23404. https://doi.org/10.1073/pnas.1907576116.

(17)   Jaffe, A.; Lin, Y.; Mao, W. L.; Karunadasa, H. I. Pressure-Induced Conductivity and Yellow-to-Black Piezochromism in a Layered Cu–Cl Hybrid Perovskite. *J. Am. Chem. Soc.* **2015**, *137*, 1673–1678. https://doi.org/10.1021/ja512396m.

(18)   Wang, S.; Hirai, S.; Shapiro, M. C.; Riggs, S. C.; Geballe, T. H.; Mao, W. L.; Fisher, I. R. Pressure-Induced Symmetry Breaking in Tetragonal $CsAuI_3$. *Phys. Rev. B* **2013**, *87*, 54104. https://doi.org/10.1103/PhysRevB.87.054104.

(19)   Gao, M.; Zhang, Y.; Lin, Z.; Jin, J.; Folgueras, M. C.; Yang, P. The Making of a Reconfigurable Semiconductor with a Soft Ionic Lattice. *Matter* **2021**, *4*, 3874–3896. https://doi.org/10.1016/j.matt.2021.09.023.

(20)   Stoumpos, C. C.; Malliakas, C. D.; Peters, J. A.; Liu, Z.; Sebastian, M.; Im, J.; Chasapis, T. C.; Wibowo, A. C.; Chung, D. Y.; Freeman, A. J. *et al.* Crystal Growth of the Perovskite Semiconductor $CsPbBr_3$: A New Material for High-Energy Radiation Detection. *Crys. Growth Des.* **2013**, *13*, 2722–2727. https://doi.org/10.1021/cg400645t.

(21)   Mao, L.; Stoumpos, C. C.; Kanatzidis, M. G. Two-Dimensional Hybrid Halide Perovskites: Principles and Promises. *J. Am. Chem. Soc.* **2018**, *141*, 1171–1190. https://doi.org/10.1021/jacs.8b10851.

(22)   Smith, M. D.; Jaffe, A.; Dohner, E. R.; Lindenberg, A. M.; Karunadasa, H. I. Structural Origins of Broadband Emission from Layered Pb–Br Hybrid Perovskites. *Chem. Sci.* **2017**, *8*, 4497–4504. https://doi.org/10.1039/C7SC01590A.

(23)   Li, X.; Fu, Y.; Pedesseau, L.; Guo, P.; Cuthriell, S.; Hadar, I.; Even, J.; Katan, C.; Stoumpos, C. C.; Schaller, R. D. *et al.* Negative Pressure Engineering with Large Cage Cations in 2D Halide Perovskites Causes Lattice Softening. *J. Am. Chem. Soc.* **2020**, *142*, 11486–11496. https://doi.org/10.1021/jacs.0c03860.

(24)   Ghaithan, H. M.; Alahmed, Z. A.; Qaid, S. M. H.; Hezam, M.; Aldwayyan, A. S. Density Functional Study of Cubic, Tetragonal, and Orthorhombic $CsPbBr_3$ Perovskite. *ACS Omega* **2020**, *5*, 7468–7480. https://doi.org/10.1021/acsomega.0c00197.

(25)   Mannino, G.; Deretzis, I.; Smecca, E.; Giannazzo, F.; Valastro, S.; Fisicaro, G.; la Magna, A.; Ceratti, D.; Alberti, A. $CsPbBr_3$, $MAPbBr_3$, and $FAPbBr_3$ Bromide Perovskite Single Crystals: Interband Critical Points under Dry N_2 and Optical Degradation under Humid Air. *J. Phys. Chem. C* **2021**, *125*, 4938–4945. https://doi.org/10.1021/acs.jpcc.0c10144.

(26)   Zhang, Y.; Parsonnet, E.; Fernandez, A.; Griffin, S. M.; Huyan, H.; Lin, C.-K.; Lei, T.; Jin, J.; Barnard, E. S.; Raja, A. *et al.* Ferroelectricity in a Semiconducting All-Inorganic Halide Perovskite. *Sci. Adv.* **2022**, *8*, eabj5881. https://doi.org/10.1126/sciadv.abj5881.

(27)   Fabini, D. H.; Laurita, G.; Bechtel, J. S.; Stoumpos, C. C.; Evans, H. A.; Kontos, A. G.; Raptis, Y. S.; Falaras, P.; Van der Ven, A.; Kanatzidis, M. G. *et al.* Dynamic Stereochemical Activity of

the Sn^{2+} Lone Pair in Perovskite $CsSnBr_3$. *J. Am. Chem. Soc.* **2016**, *138*, 11820–11832. https://doi.org/10.1021/jacs.6b06287.

(28) McCall, K. M.; Morad, V.; Benin, B. M.; Kovalenko, M. v. Efficient Lone-Pair-Driven Luminescence: Structure–Property Relationships in Emissive $5s^2$ Metal Halides. *ACS Mater. Lett.* **2020**, *2*, 1218–1232. https://doi.org/10.1021/acsmaterialslett.0c00211.

(29) Morad, V.; Yakunin, S.; Benin, B. M.; Shynkarenko, Y.; Grotevent, M. J.; Shorubalko, I.; Boehme, S. C.; Kovalenko, M. v. Hybrid 0D Antimony Halides as Air-Stable Luminophores for High-Spatial-Resolution Remote Thermography. *Adv. Mater.* **2021**, *33*, 2007355. https://doi.org/10.1002/adma.202007355.

(30) Bass, K. K.; Estergreen, L.; Savory, C. N.; Buckeridge, J.; Scanlon, D. O.; Djurovich, P. I.; Bradforth, S. E.; Thompson, M. E.; Melot, B. C. Vibronic Structure in Room Temperature Photoluminescence of the Halide Perovskite $Cs_3Bi_2Br_9$. *Inorg. Chem.* **2016**, *56*, 42–45. https://doi.org/10.1021/acs.inorgchem.6b01571.

(31) Liu, C.; Wang, Y.; Geng, H.; Zhu, T.; Ertekin, E.; Gosztola, D.; Yang, S.; Huang, J.; Yang, B.; Han, K. *et al.* Asynchronous Photoexcited Electronic and Structural Relaxation in Lead-Free Perovskites. *J. Am. Chem. Soc.* **2019**, *141*, 13074–13080. https://doi.org/10.1021/jacs.9b04557.

(32) Dotsenko, A. A.; Vovna, V. I.; Korochentsev, V. v.; Mirochnik, A. G.; Shcheka, O. L.; Sedakova, T. v.; Sergienko, V. I. Halide Perovskite-Derived Compounds Rb_2TeX_6 (X = Cl, Br, and I): Electronic Structure of the Ground and First Excited States. *Inorg. Chem.* **2019**, *58*, 6796–6803. https://doi.org/10.1021/acs.inorgchem.9b00250.

(33) Folgueras, M. C.; Jin, J.; Gao, M.; Quan, L. N.; Steele, J. A.; Srivastava, S.; Ross, M. B.; Zhang, R.; Seeler, F.; Schierle-Arndt, K. *et al.* Lattice Dynamics and Optoelectronic Properties of Vacancy-Ordered Double Perovskite Cs_2TeX_6 (X = Cl^-, Br^-, I^-) Single Crystals. *J. Phys. Chem. C* **2021**, *125*, 25126–25139. https://doi.org/10.1021/acs.jpcc.1c08332.

(34) Ju, D.; Zheng, X.; Yin, J.; Qiu, Z.; Türedi, B.; Liu, X.; Dang, Y.; Cao, B.; Mohammed, O. F.; Bakr, O. M. *et al.* Tellurium-Based Double Perovskites A_2TeX_6 with Tunable Band Gap and Long Carrier Diffusion Length for Optoelectronic Applications. *ACS Energy Lett.* **2018**, *4*, 228–234. https://doi.org/10.1021/acsenergylett.8b02113.

(35) Stufkens, D. J. Dynamic Jahn-Teller Effect in the Excited States of $SeCl_6^{2-}$, $SeBr_6^{2-}$, $TeCl_6^{2-}$ and $TeBr_6^{2-}$: Interpretation of Electronic Absorption and Raman Spectra. *Recueil des Travaux Chimiques des Pays-Bas* **1970**, *89*, 1185–1201. https://doi.org/10.1002/recl.19700891109.

(36) Xiao, Z.; Song, Z.; Yan, Y. From Lead Halide Perovskites to Lead-Free Metal Halide Perovskites and Perovskite Derivatives. *Adv. Mater.* **2019**, *31*, 1803792. https://doi.org/10.1002/adma.201803792.

(37) Shi, M.; Yang, B.; Liu, S.; Zhang, R.; Han, K.; Li, C.; Li, R. Tuning Exciton Recombination Pathways in Inorganic Bismuth-Based Perovskite for Broadband Emission. *Energy Material Advances* **2022**, *2022*, 9845942. https://doi.org/10.34133/2022/9845942.

(38) McCall, K. M.; Stoumpos, C. C.; Kontsevoi, O. Y.; Alexander, G. C. B.; Wessels, B. W.; Kanatzidis, M. G. From 0D $Cs_3Bi_2I_9$ to 2D $Cs_3Bi_2I_6Cl_3$: Dimensional Expansion Induces a Direct Band Gap but Enhances Electron–Phonon Coupling. *Chem. Mater.* **2019**, *31*, 2644–2650. https://doi.org/10.1021/acs.chemmater.9b00636.

(39) McCall, K. M.; Stoumpos, C. C.; Kostina, S. S.; Kanatzidis, M. G.; Wessels, B. W. Strong Electron–Phonon Coupling and Self-Trapped Excitons in the Defect Halide Perovskites $A_3M_2I_9$

(A = Cs, Rb; M = Bi, Sb). *Chem. Mater.* **2017**, *29*, 4129–4145. https://doi.org/10.1021/acs.chemmater.7b01184.

(40) Shi, M.; Li, G.; Tian, W.; Jin, S.; Tao, X.; Jiang, Y.; Pidko, E. A.; Li, R.; Li, C. Understanding the Effect of Crystalline Structural Transformation for Lead-Free Inorganic Halide Perovskites. *Adv. Mater.* **2020**, *32*, 2002137. https://doi.org/10.1002/adma.202002137.

(41) Baranowski, M.; Plochocka, P. Excitons in Metal-Halide Perovskites. *Adv. Energy Mater.* **2020**, *10*, 1903659. https://doi.org/10.1002/aenm.201903659.

(42) *CrysAlisPro 1.171.39.45f*. (Rigaku Oxford Diffraction, 2018).

(43) Dolomanov, O. v; Bourhis, L. J.; Gildea, R. J.; Howard, J. A. K.; Puschmann, H. OLEX2: A Complete Structure Solution, Refinement and Analysis Program. *J. Appl. Cryst.* **2009**, *42*, 339–341. https://doi.org/10.1107/S0021889808042726.

(44) Sheldrick, G. M. SHELXT – Integrated Space-Group and Crystal-Structure Determination. *Acta Cryst. A* **2015**, *71*, 3–8. https://doi.org/10.1107/S2053273314026370.

(45) Sheldrick, G. M. Crystal Structure Refinement with SHELXL. *Acta Cryst. C* **2015**, *71*, 3–8. https://doi.org/10.1107/S2053229614024218.

(46) Holtgrewe, N.; Greenberg, E.; Prescher, C.; Prakapenka, V. B.; Goncharov, A. F. Advanced Integrated Optical Spectroscopy System for Diamond Anvil Cell Studies at GSECARS. *High Press. Res.* **2019**, *39*, 457–470. https://doi.org/10.1080/08957959.2019.1647536.

(47) Clark, S. J.; Segall, M. D.; Pickard, C. J.; Hasnip, P. J.; Probert, M. I. J.; Refson, K.; Payne, M. C. First Principles Methods Using CASTEP. *Z. Kristallogr.* **2005**, *220*, 567–570. https://doi.org/10.1524/zkri.220.5.567.65075.

(48) Hamann, D. R.; Schlüter, M.; Chiang, C. Norm-Conserving Pseudopotentials. *Phys. Rev. Lett.* **1979**, *43*, 1494–1497. https://doi.org/10.1103/PhysRevLett.43.1494.

(49) Kohn, W.; Sham, L. J. Self-Consistent Equations Including Exchange and Correlation Effects. *Phys. Rev.* **1965**, *140*, A1133–A1138. https://doi.org/10.1103/PhysRev.140.A1133.

(50) Polik, W. F.; Schmidt, J. R. WebMO: Web-Based Computational Chemistry Calculations in Education and Research. *WIREs Comput. Mol. Sci.* **2022**, *12*, e1554. https://doi.org/10.1002/wcms.1554.

(51) Schlegel, H. B. Optimization of Equilibrium Geometries and Transition Structures. *J Comput. Chem.* **1982**, *3*, 214–218. https://doi.org/10.1002/jcc.540030212.
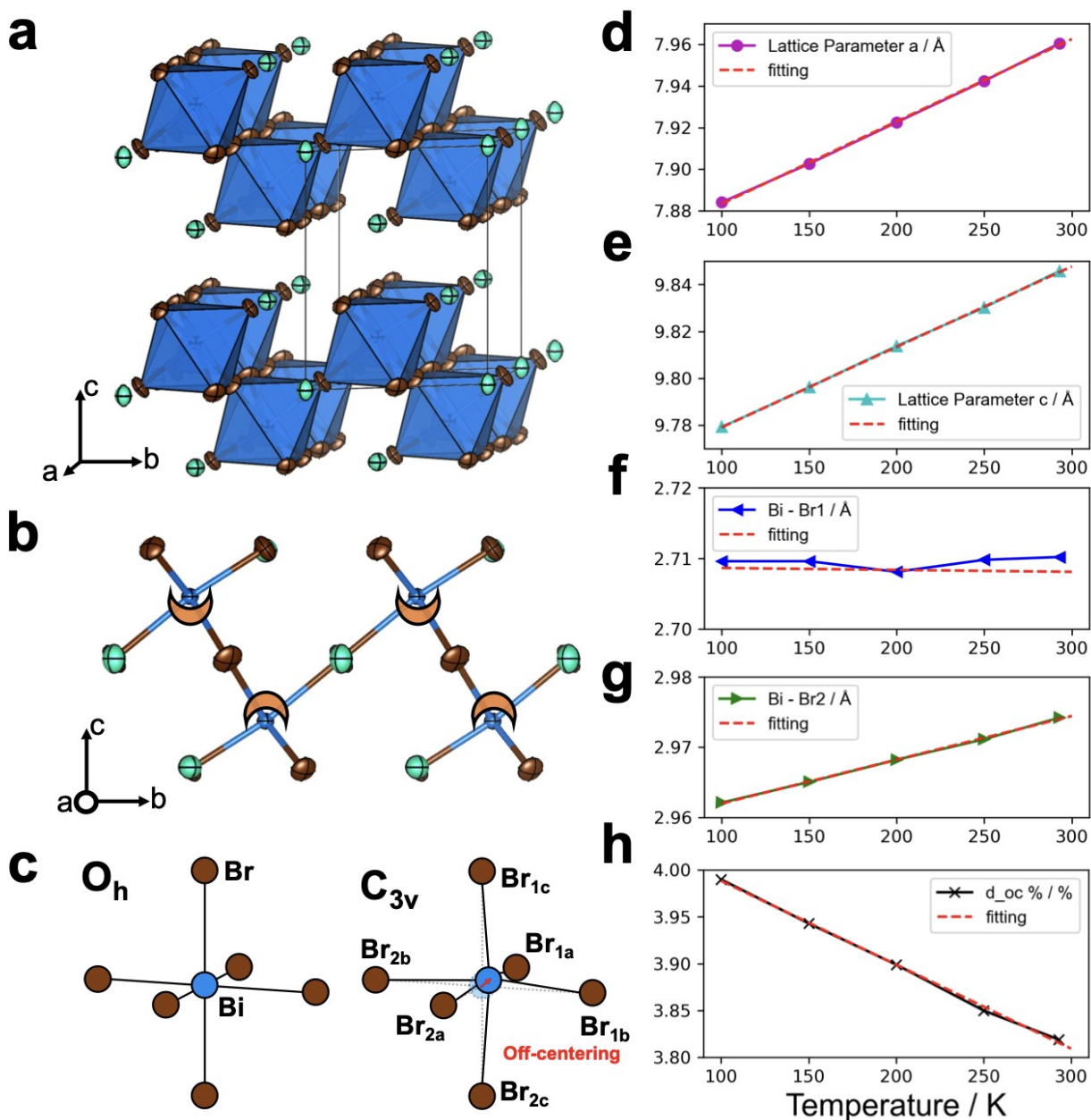
Figure 1: Lattice Structure and Octahedron Distortions of Cs₃Bi₂Br₉ from room temperature to 100 K.

(a) The layered structure of $Cs_3Bi_2Br_9$, (b) the off-centering of Bi^{3+} within single $[BiBr_6]^{3-}$ octahedron are along the c axis of the trigonal unit cell, (c) The $[BiBr_6]^{3-}$ octahedron model in O_h and C_{3v} point group, the red arrow shows the off-centering vectors (d_{oc}). (d-h) The changes of lattice parameters a, c, Bi-Br$_1$ bond length, Bi-Br$_2$ bond length, and degree of off-centering (d_{oc} %) of $Cs_3Bi_2Br_9$ from room temperature to 100 K.

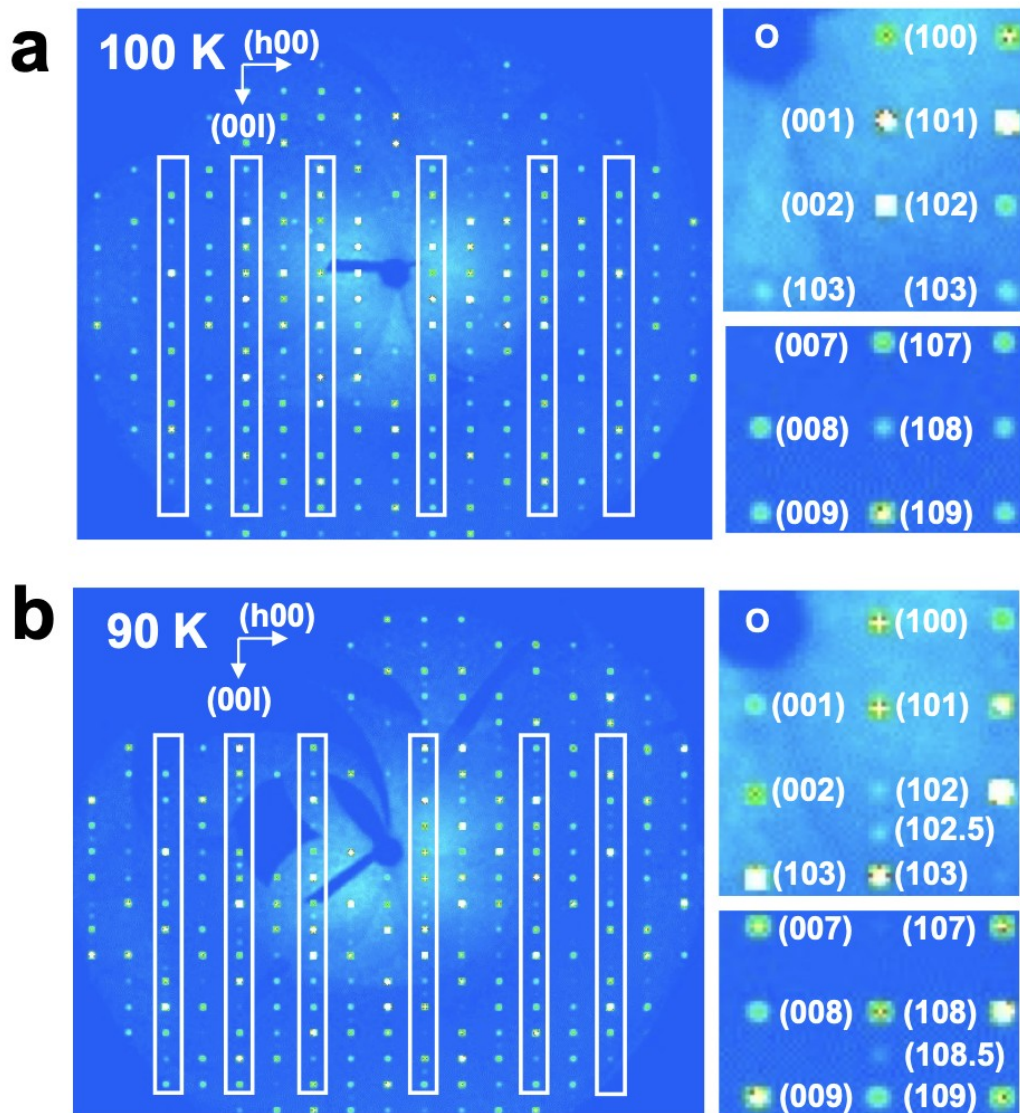**Figure 2: The Diffraction Patterns of Cs$_3$Bi$_2$Br$_9$ at 100 K and 90 K.**
Unwarp images built on (100) and (001) layers based on P-3m1 unit cell of Cs$_3$Bi$_2$Br$_9$ at 100 K
(a) and 90 K (b). The white boxes highlighted the region where additional diffractions appear.
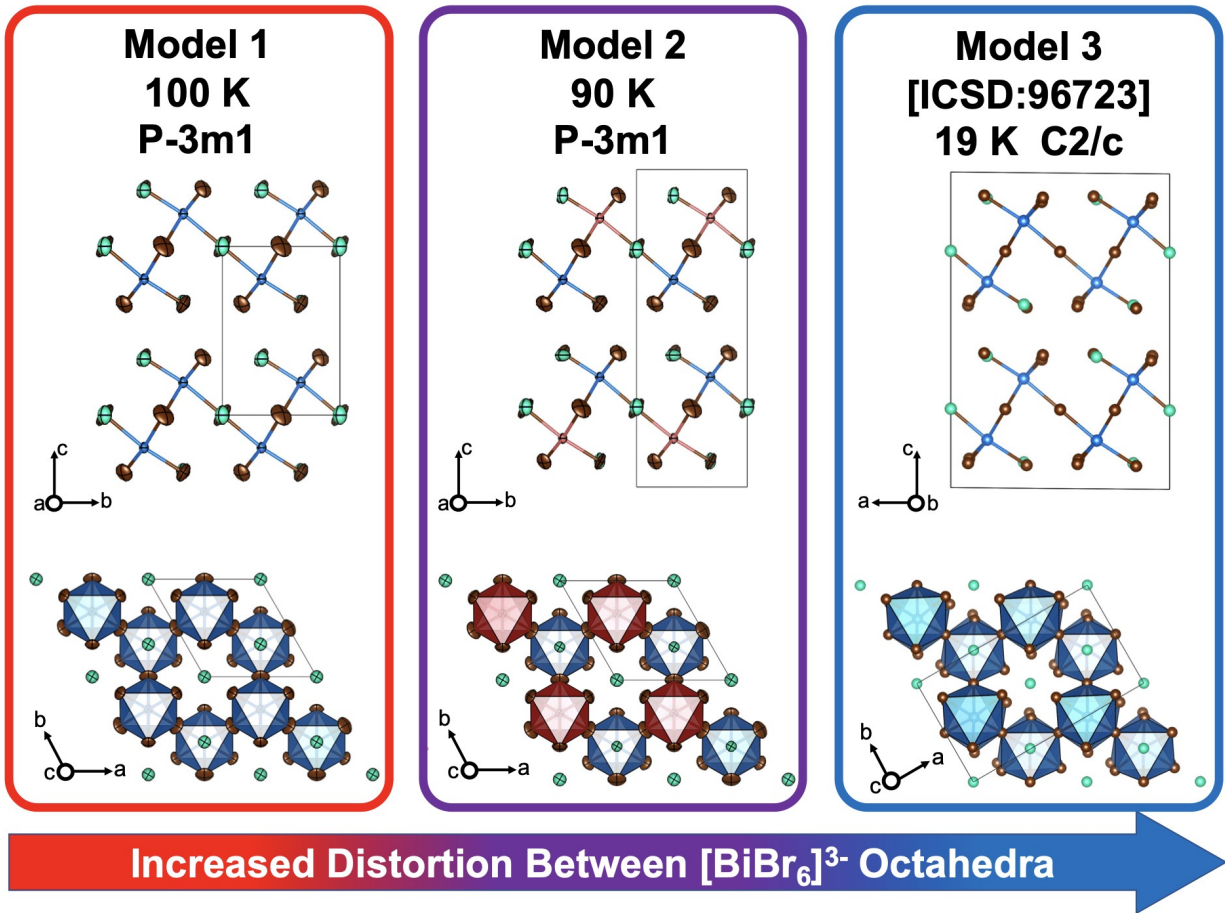The side figures show the occurrence of (1,0,2.5) and (1,0,8.5) peaks.

Figure 3: Phase Transitions and Octahedron Distortions of Cs$_3$Bi$_2$Br$_9$ below 100 K.

The side view and top view of the prototype P-3m1 unit cell (100 K, Model 1), the doubled P-3m1 unit cell (90 K, Model 2) and the quadruple monoclinic C2/c unit cell (19 K, Model 3, ICSD-96723[11]). [highlighting the unit cell expanding as a direct consequence of inter-unit distortion]
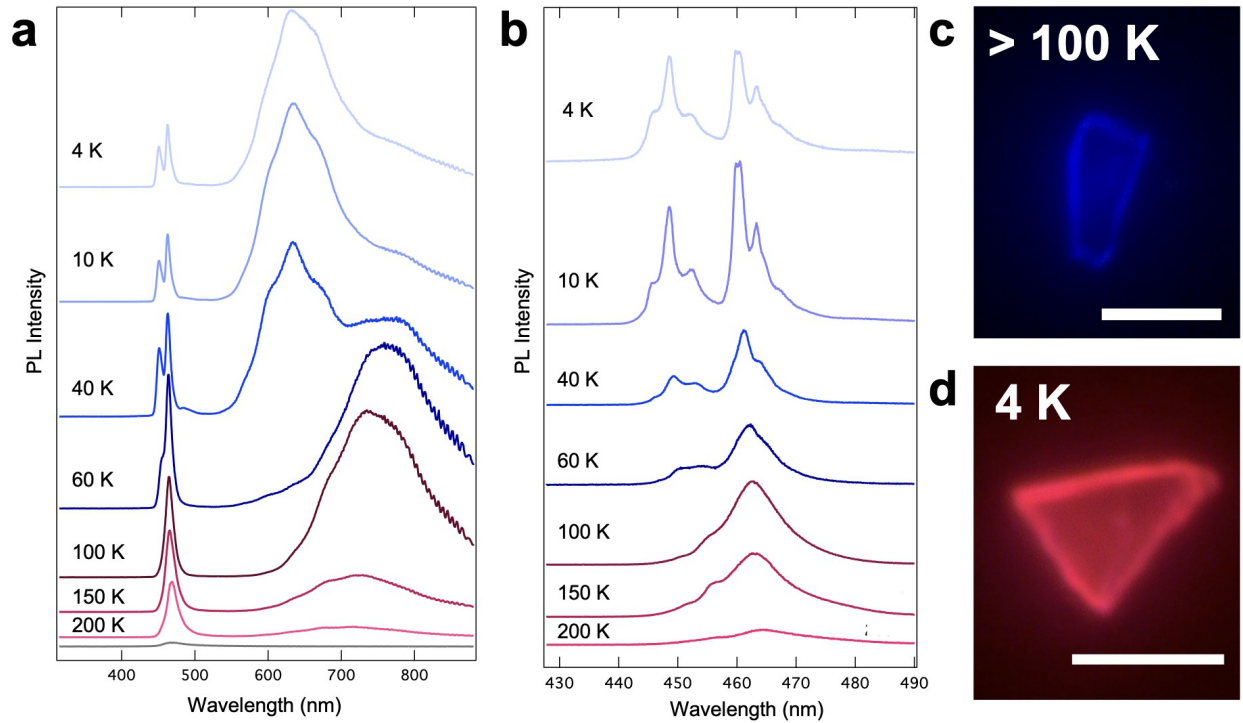
Figure 4: Temperature-dependent Optical Measurements on Cs₃Bi₂Br₉.
(a-b) Temperature-dependent photoluminescence spectra (a, 150 gr/mm, b, 1200 gr/mm) of Cs$_3$Bi$_2$Br$_9$ from room temperature to 4 K. (c-d) Optical microscope images of the blue emissions above 100 K and the red emissions at 4 K under laser excitation (375nm), scale bar: 20µm .
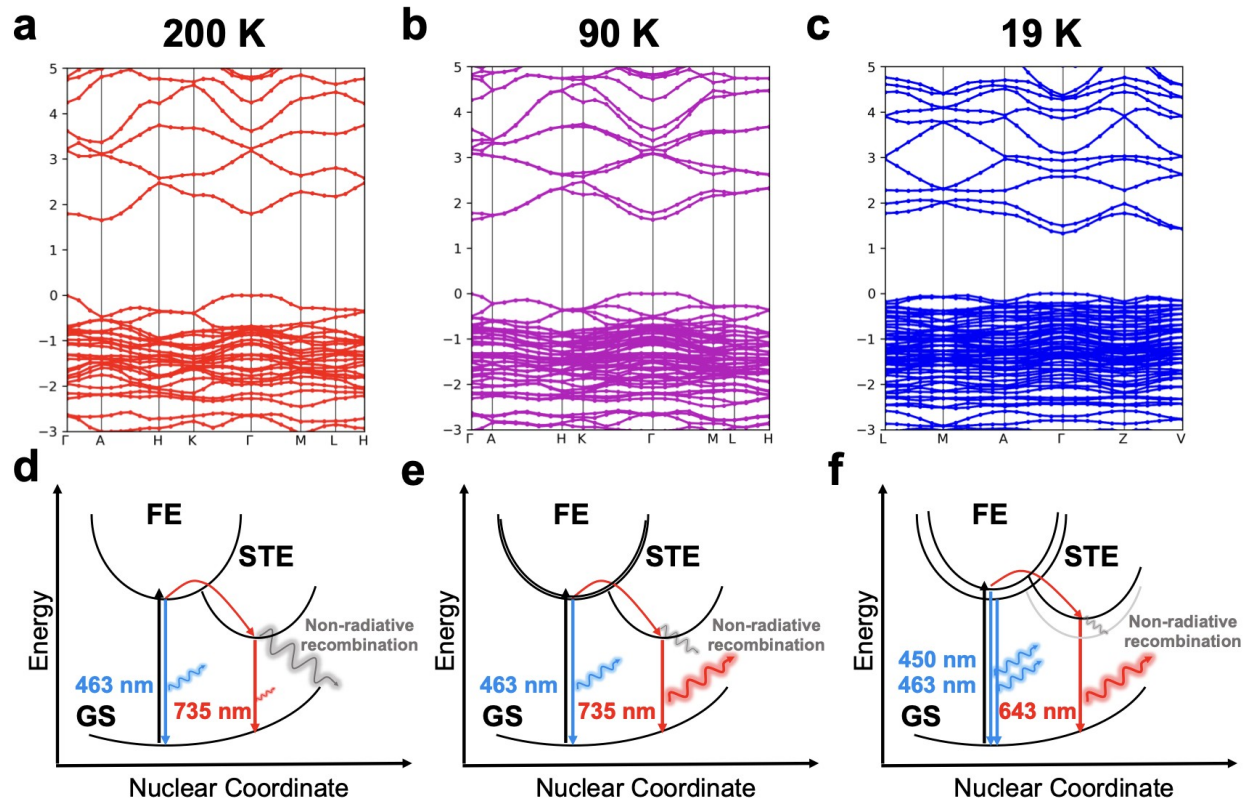
Figure 5: Band Structures and Schematics for Exciton Behaviors of Cs₃Bi₂Br₉.
(a, d) DFT calculated band structures and the schematics for Exciton behaviors of prototype P-3m1 unit cell of Cs₃Bi₂Br₉ at 200 K, (b, e) DFT calculated band structures and the schematics for Exciton behaviors of doubled trigonal P-3m1 unit cell of Cs₃Bi₂Br₉ at 90 K. (c, f) DFT calculated band structures and the schematics for Exciton behaviors of the primitive cell quadruple monoclinic C2/c unit cell of Cs₃Bi₂Br₉ at 19 K.

Tables of Contents

Intra-octahedral distortion   Inter-octahedral distortion

$[BiBr_6]^{3-}$ ionic octahedron in $Cs_3Bi_2Br_9$

Centered → Off-centered   Aligned → Misaligned

Excitonic Behavior

> 100 K → 4 K